Two-Dimensional Model of Methane Thermal Decomposition Reactors with Radiative Heat Transfer and Carbon Particle Growth

Cyril Caliot and Gilles Flamant
Processes, Materials, and Solar Energy Laboratory, PROMES-CNRS, Centre F. Trombe, 7 Rue du Four Solaire, 66120 Odeillo Font-Romeu, France

Giorgos Patrianakos
Aerosol and Particle Technology Laboratory (APTL), Chemical Process Engineering Research Institute (CPERI), Centre for Research and Technology Hellas (CERTH), 6th km Charilaou - Thermi Road, Thermi 57001, Thessaloniki, Greece

Margaritis Kostoglou
Dept. of Chemistry, Aristotle University of Thessaloniki, University Box 116, Thessaloniki 54124, Greece

Athanasios G. Konstandopoulos
Dept. of Chemical Engineering, Aristotle University of Thessaloniki, P. O. Box 1517, Thessaloniki 54006, Greece

DOI 10.1002/aic.12767
Published online October 11, 2011 in Wiley Online Library (wileyonlinelibrary.com).

A two-dimensional model of methane thermal decomposition reactors is developed which accounts for coupled radiative heat and polydisperse carbon particle nucleation, growth, and transport. The model uses the Navier–Stokes equations for the fluid dynamics, the radiative transfer equation for methane and particle species radiation absorption, the advection–diffusion equation for gas and particle species transport, and a sectional method for particle species nucleation, heterogenous growth, and coagulation. The model is applied to a tubular laminar flow reactor. The simulation results indicate the development of a reaction boundary layer inside the reactor, which results in significant variation of the local particle size distribution across the reactor. © 2011 American Institute of Chemical Engineers *AIChE J,* 58: 2545–2556, 2012
Keywords: heat transfer, mass transfer, computational fluid dynamics, nucleation, particulate flows

Introduction

Concentrated solar radiation is an energy source suitable for the production of renewable hydrogen using high temperature thermochemical processes. In particular, the solar thermal decomposition of methane (TDM) is one possible route for the production of hydrogen with zero carbon dioxide emissions.[1] The TDM by concentrated solar energy has recently been investigated experimentally using indirect and direct solar heating modes to decompose methane. In the case of indirect heating, Abanades and co-workers investigated multitubular reactors,[2,3] while Dahl et al.[4,5] studied a tubular fluid wall aerosol reactor. In the case of direct heating, Kogan et al.[6–8] proposed and studied a conical tornado flow reactor, while Steinfeld and co-workers[9,10] investigated a cylindrical vortex flow reactor. Direct heating mode reactors are based on a combined cavity receiver reactor in which the gas flow is laden with so-called ''seed'' particles that absorb the incident solar radiation and heat the gas; as such, direct heating mode reactors require a transparent window to allow the solar radiation into the reactor. On the other hand, in the case of indirect heating mode reactors, the solar radiation is absorbed externally by the opaque walls of the reactor which then transfer heat to the gas via convection and radiation exchange with the gas; as such, seeding is not strictly necessary in indirect heating mode reactors, although it may be used to improve wall gas heat transfer, e.g. Ref. 4 and 5. In direct heating mode reactors, the seed particles can offer a large surface area for radiation absorption throughout the depth of the reactor; however, there is the risk of window darkening and overheating due to particle deposition.

Several kinetic studies have been performed to identify kinetic parameters for methane decomposition reaction in solar thermal reactors[11–16]; these studies have been based on experimental results, and, thus, the kinetic parameters obtained are specific to particular reactors. Recently, Ozalp and Shilapuram[17] performed a thermodynamic study to compare the different kinetic parameters obtained by Rodat et al.,[14] Trommer et al.,[12] and Wyss et al.[13]

Several simulation studies of solar thermal methane decomposition reactors have also been performed. Abanades and Flamant[18] performed two-dimensional (2-D) simulations

Correspondence concerning this article should be addressed to C. Caliot at cyril.Caliot@promes.cnrs.fr or G. Flamant at Gilles.Flamant@promes.cnrs.fr.

of an indirectly heated tubular reactor to predict the temperature, species concentration, and reaction extent inside the reactor. The model addressed coupled heat and mass transfer by solving the Navier–Stokes equations, and it accounted for radiation absorption by the tube, conjugate heat conduction in the tube walls, wall gas convection, and homogenous reaction in the gas. To compute radiation transport, the gas particle mixture was treated as one semi transparent phase. Dahl et al.[19] developed a one-dimensional (1-D), nonisothermal model of an indirectly heated, seeded reactor, in which the particle phase was treated as a variable number, constant diameter, monodisperse particle population, and which included a gray radiation model for wall particle radiation exchange. Hirsch and Steinfeld[20] developed a three-dimensional radiative heat transfer model for a directly heated, seeded, vortex flow reactor, which employed Mie theory to account for the absorption and scattering of radiation by the seed particles. Radiation transport in the reactor was modeled using a Monte Carlo method, in which the particles were treated as a constant diameter, monodisperse particle population. The radiative transfer model was coupled to conduction, convection, and chemical reaction models, but the flow dynamics was not solved. A 1-D transient model was also developed for this reactor by Maag et al.,[21] in which the unsteady mass and energy conservation equations were solved, accounting for the coupling between convective heat transfer, radiative heat transfer, and chemical reaction. Separate gas and particle phases were considered at different temperatures, and the heterogenous decomposition of methane on the surface of the particles was addressed. The particle phase was treated as a constant number, variable diameter, monodisperse particle population. Radiation transport was modeled in the gas and particle phases, as before, using a Monte Carlo method. Mie theory was used to calculate the scattering and absorption of radiation by the particles, and the Hitran-2004 database for low temperature spectra was used for the absorption of radiation by methane. Ozalp and Shilapuram[17] developed a Lagrangian model to track the seed particles in a directly heated, tornado flow reactor, and to study their concentration and deposition on the walls of the reactor. Lastly, Patrianakos et al.[16] developed a 1-D model for indirectly heated, seeded reactors, in which the particle phase was treated as a polydisperse particle population. Homogenous reaction in the gas phase and heterogenous reaction on the surface of the particles and on the walls of the reactor were addressed. The model considered wall gas heat convection, wall particle radiation exchange and particle gas heat convection. Particle nucleation, coagulation, and deposition were also considered. The radiation absorption efficiency of the particles was calculated using Mie theory. The simulation studies briefly reviewed earlier were used to identify kinetic parameters for the decomposition reaction[16,18] and to realize sensitivity studies.[19–21]

To gain a better understanding of the radiation and particle transport phenomena in the tubular (TDM) reactors developed by the PROMES laboratory, it is necessary to integrate accurate radiation transport and polydisperse particle population models into a multidimensional fluid dynamics model of the reactors. To this end, the present work describes a model coupling these phenomena, which uses the Navier–Stokes equations to address the fluid dynamics, the energy conservation equation to address heat transport in the combined gas and particle flow, the radiative heat transfer equation to address methane and carbon particle radiation absorption at high temperatures, the advection–diffusion equation to address gas and particle species transport, and a sectional method to address particle species nucleation, heterogenous growth, and coagulation. This approach enables the coupled effect of radiation absorption and particle formation and growth to be resolved spatially throughout the reactor at moderate computational cost. Furthermore, the model is implemented in a 2-D axisymetrical discretization of the reactor geomety, and, in the way of a first application, it is used to simulate the reactor tube of a multitubular 50 kW TDM reactor developed by PROMES[3] to investigate on a qualitative basis the interaction between radiation transport and particle formation and growth.

The remainder of the article is organized as follows: first, the mathematical formulation of the model is discussed, covering fluid dynamics, radiation transport, and particle transport; second, the computational implementation of the model is discussed, covering the applied numerical methods, the computational domain, and the treatment of boundary conditions; third, the simulation results are then discussed, covering particular aspects related to radiation transport and particle transport; finally, conclusions are drawn.

Mathematical Formulation of the Model

Fluid dynamics model

The following single-step reaction is considered for the TDM

$$CH_4 \longrightarrow 2H_2 + C(s) \tag{1}$$

The flow inside the reactor is composed of submicron carbon particles suspended in a gas mixture. On account of the small size of the particles and of the small volume fraction of the particle population [$O(10^{-5})$], the Stokes number of the particles is much less than one and the velocity of the particles is approximately the same as that of the gas. Furthermore, the surface area of the particles available for particle gas heat convection is large compared to the thermal inertia of the particles, and, consequently, the gas and particle temperatures are approximately identical. As such, for the purpose of solving the flow dynamics, the gas particle mixture is treated as a single fluid phase in dynamic and thermal equilibrium, and a homogenous model is used for the Navier–Stokes equations. Therefore, within an Eulerian framework, the flow dynamics is modeled using the following steady state conservation equations for mass (Eq. 2), momentum (Eq. 3), energy (Eq. 4), and species mass (Eq. 5) transport

$$\frac{\partial}{\partial x_l}(\rho u_l) = 0 \tag{2}$$

$$\frac{\partial(\rho u_l u_k)}{\partial x_l} = -\frac{\partial p}{\partial x_k} + \mu \frac{\partial^2 u_l}{\partial x_l^2} \tag{3}$$

$$\frac{\partial}{\partial x_l}(\rho u_l h) = \frac{\partial}{\partial x_l}\left(\lambda \frac{\partial T}{\partial x_l} - \sum_n h_n J_{n,l}\right) + S_{\text{chem}} + S_{\text{rad}} \tag{4}$$

$$\frac{\partial}{\partial x_l}(\rho u_l Y_n) = \frac{\partial}{\partial x_l}\left(\rho D_{n,\text{g}} \frac{\partial Y_n}{\partial x_l}\right) + R_n \tag{5}$$

$$h = \sum_n Y_n h_n \;\; ; \;\; h_n = \int_{T_r}^{T} C_{p,n} dT$$

where the density ρ, thermal conductivity λ, and sensible enthalpy h are those of the gas particle mixture. However, the viscosity μ is that of the gas phase alone, as the particle phase is discontinuous, and no gas particle, or particle particle, forces are assumed. The source term S_{chem} in the energy transport equation (Eq. 4) accounts for the heat release from chemical reaction, including homogenous reaction in the gas phase and heterogenous reaction on the surface of the particles, whereas the source term S_{rad} accounts for the radiation absorbed and emitted by the methane and the carbon particles. Separate species transport equations (Eq. 5) are formulated for each of the gas and particle species considered. The source term R_n accounts for the net rate of consumption or production of the n-th species by homogenous reaction, heterogenous reaction and coagulation (in the case of particle species). The source terms R_n for the particle species are discussed in greater detail in the "Particle transport model" section.

The gas phase is treated as a gas mixture composed of the gaseous species Ar, CH_4, and H_2. Ideal gas behavior is assumed for both the mixture and its constituent species. The specific heat capacity, thermal conductivity, and viscosity of Ar were extracted from the work of Ref. 22. The specific heat capacities of CH_4 and H_2 were obtained from the HSC software,[23] and the thermal conductivities and viscosities were obtained from the Component Plus database.[24] The temperature dependence of the gaseous species' thermophysical properties is described where necessary using polynomial functions. The thermal conductivity and viscosity of the gas mixture are calculated using the semi empirical mixture rule of Wilke.[25] The thermal conductivity of the gas particle mixture is calculated using a parallel model for the gas phase conductivity λ_g and particle phase conductivity λ_p: $\lambda^{-1} = f_v/\lambda_p + (1 - f_v)/\lambda_g$, where f_v is the volume fraction of the particles. On account of the small volume fraction of the particles, it is apparent that the conductivity of the gas particle mixture is essentially that of the gas phase. The Brownian diffusivity of the gas species with respect to the gas mixture is calculated using the Chapman–Enskog equation for dilute species and the Lennard-Jones function to approximate the intermolecular potential field.[25] The Brownian diffusivity of the particles is calculated using the Stokes–Einstein equation with the inclusion of a slip correction factor to account for kinetic and transition regime effects.[16] Thermophoretic diffusion of the particles is currently not considered in the model: on the basis of the temperature gradients simulated in the reactor and using Brock's expression for the thermophoretic velocity of the particles,[26] the cumulative radial displacement of the particles along the reactor due to radial thermophoretic forces (the direction of maximum temperature gradient) is less than 5% of the reactor radius.

Radiation transport model

Radiation transport is considered in an emitting, absorbing, nonscattering, and nongray medium surrounded by gray walls. The monochromatic radiative transfer equation (RTE) for an absorbing and emitting medium, at position $\vec{r}$ and in the direction $\vec{s}$, can be written as

$$\frac{dI_v}{ds} = \kappa_v (I_{bv} - I_v) \tag{6}$$

The boundary condition involving a gray surface that emits and reflects diffusely is given by

$$I_{wv}(\vec{s}) = \varepsilon_w I_{bv} + \frac{1 - \varepsilon_w}{\pi} \int_{\vec{n}\cdot\vec{s}'<0} |\vec{n}\cdot\vec{s}'| I_v(\vec{s}') d\Omega' \tag{7}$$

The radiative property model chosen in this study is a multigray approach and the RTE for the jth gray component is expressed as[27]

$$\frac{dI_j}{ds} = \kappa_j \left(a_j \frac{\sigma T^4}{\pi} - I_j \right) \tag{8}$$

where a_j and κ_j are, respectively, the emission weighting factor and absorption coefficient for the jth gray component. The quantities a_j and κ_j are temperature dependent. The boundary conditions for gray walls thus become

$$I_w(\vec{s}) = \varepsilon_w a_j \frac{\sigma T^4}{\pi} + \frac{1 - \varepsilon_w}{\pi} \int_{\vec{n}\cdot\vec{s}'<0} |\vec{n}\cdot\vec{s}'| I_j(\vec{s}') d\Omega' \tag{9}$$

The RTE (Eq. 8) is solved using the discrete ordinates (DO) radiation model (as it is called in the ANSYS Fluent commercial software) for a finite number of discrete angles. The DO model corresponds to the finite-volume method developed by Raithby and Chui.[28] In 2-D simulations, only four octants are solved due to symmetry. In the following 2-D simulations, 16 directions are adopted for the angular discretization of each octant.

The participating medium is a methane carbon particle mixture at high temperature. During a preliminary study concerning the influence of radiation in the preheating zone of a tubular TDM reactor,[29] a non negligible increase in the temperature of the gas mixture (in this case a CH_4, Ar mixture) due to methane absorption was found, and, therefore, the absorption and emission of radiation by both methane and carbon particles is modeled in the present work. The absorption distribution function (ADF) model[30] is used as the global spectral model for methane at high temperature (ADF-CH_4), as derived from the narrow band radiative properties of methane at high temperature provided by Perrin and Soufiani.[31] A detailed description of the ADF-CH_4 model can be found in Caliot et al.[29] As the particle phase is dilute, independent absorption of radiation by the particles is assumed. Mie theory is used to calculate the mean Planck absorption coefficient of the particle population, as the size parameter (Pi times the ratio between the particle diameter and the wavelength) of the particles ranges roughly between 10^{-2} and 10. A mean value of the absorption coefficient is obtained by spectral integration for each particle size considered in the adopted sectional method and subsequent averaging over the particle size distribution (see the "Particle transport model" section). The ADF model is also used as the spectral model for the gas particle mixture. The jth gray absorption coefficient of the gas particle mixture is taken as the sum of the mean absorption coefficient of the particle population and the gray gas absorption coefficient from the ADF-CH_4 model; the weighting factors are the same as those in the ADF-CH_4 model.

Particle transport model

Polydisperse particle population models have been used for many years to simulate particle nucleation and coagulation phenomena in aerosol reactors,[32] for example the

Lagrangian reactor model of Pratsinis,[33] using a moment method based particle model and the 1-D Eulerian reactor model of Xiong and Pratsinis,[34] using a sectional method based particle model. Furthermore, many of the particle formation processes occuring in the TDM reactors considered in the present work are similar to those occurring in the sooting flames of Diesel compression ignition engines, since both cases involve, *albeit* to a different extent, pyrolysis of the feedstock hydrocarbon to higher molecular weight poly aromatic hydrocarbons, considered particle precursors, which subsequently form carbonaceous particles via a so-called hydrogen abstraction carbon addition process, in which acetylene is understood to play a significant role.[35,36] Of course, oxidation reactions that affect particle growth (e.g., oxidative attrition and fragmentation) are also present in Diesel engines but not in TDM reactors; nevertheless, there is significant commonality between many of the basic particle formation mechanisms in the two processes. The flame structure and soot formation processes in Diesel engines have been studied in detail using models of varying dimensionality and complexity in the used chemical reaction and particle population models. For example, Frenklach and Wang[36] developed a 1-D flame model using a multi species reaction model coupled to a polydisperse moment method-based particle model; Richter et al.[37] developed a 1-D flame model using a multi species reaction model coupled to a polydisperse sectional method-based particle model; Tao et al.[38] developed a 2-D flame model use a nine-step phenomenological reaction model coupled to a monodisperse particle model; Tao et al.[39] developed a 2-D flame model using a multi species reaction model coupled to a monodisperse particle population model; Hong et al.[40] developed a 2-D flame model using a multi species reaction model coupled to a polydisperse moment method-based particle model. Implementing polydisperse particle population models in multidimensional fluid dynamics reactor models is in general computationally costly. In particular, a trade-off exists between moment method-and sectional method-based models: the particle size distribution is modeled with fewer degrees of freedom in the former method compared to the latter and, therefore, moment method-based models are computationally cheaper but less accurate than sectional method-based models.

To more accurately study the formation and growth of carbon particles in TDM reactors, and to predict the size distribution of the product particles at the exit of the reactor, a polydisperse particle population model is therefore required. Within the context of the present 2-D fluid dynamics reactor model, a sectional method is used, based on the work of Patrianakos et al.,[16] on the premise that the particle size distribution varies significantly throughout the reactor and, therefore, the flexibility of a sectional method is required to capture with any accuracy the coupling between radiative heat transfer and particle formation and growth. The particle model is used in conjunction with a one-step phenomenological reaction model in which the homogenous decomposition of methane is assumed to result in the nucleation of single carbon atoms (or monomers) which subsequently evolve into a polydisperse population of larger particles (or *i*-mers) via coagulation and heterogenous decomposition of methane on the surface of the particles. The decomposition reaction could be modeled using a multistep reaction mechanism, allowing, in particular, the concentration of gaseous by-product species in the off-gas of the reactor (such as acetylene) to be predicted; however, this would add complexity in terms of the kinetic parameters required, and, to a first approximation, it is not necessary to model the evolution of the particle size distribution inside the reactor as this is influenced mostly by the coagulation process.

A sectional method[41] is applied based on the number concentration of the particles in each section N_i, in which the pivot points of the sections are defined based on a geometric ratio of two

$$v_i = 2^{i-1} v_1; \quad i = 1, \ldots, M \tag{10}$$

$$v_1 = \frac{\tilde{m}_C}{\rho_C \tilde{N}_A} \tag{11}$$

where spherical particles are assumed, v_i is the volume of each particle in the ith section, and M is the number of sections considered. Assuming $\rho_C = 2270$ kg/m^3 and $M = 46$, the diameter of the particles in the last section is approximately 8 μm, and, therefore, the expected particle size range is adequately covered using $M = 46$ sections. The corresponding mass fraction of the i-mer particles is

$$Y_i = \frac{m_i N_i}{\rho} \quad ; \quad i = 1, \ldots, M \tag{12}$$

Assuming first order homogenous reaction, the monomer number source (nucleation rate) is

$$\left[\dot{N}_1\right]_{\text{hom}} = k_{\text{hom}}\, c_{CH_4}\, \tilde{N}_A \tag{13}$$

where an Arrhenius expression is assumed for the reaction rate constant

$$k_{\text{hom}} = k_{0,\text{hom}} \exp\left(-\frac{E_{a,\text{hom}}}{\tilde{R}T}\right) \tag{14}$$

Furthermore, assuming first order heterogenous reaction, the fractional volume growth rate of i-mer particles due to surface growth is

$$H_{\text{het},i} = \frac{k_{\text{het}} h_{CH_4,i}}{k_{\text{het}} + h_{CH_4,i}} \tilde{N}_A c_{CH_4} \frac{v_1}{v_i} s_i \tag{15}$$

where an Arrhenius expression is assumed for the intrinsic heterogenous reaction rate constant

$$k_{\text{het}} = k_{0,\text{het}} \exp\left(\frac{-E_{a,\text{het}}}{\tilde{R}T}\right) \tag{16}$$

and the corresponding total volumetric heterogenous reaction rate constant is

$$k'_{\text{het}} = \sum_{i=1}^{M} \frac{k_{\text{het}} h_{CH_4,i}}{k_{\text{het}} + h_{CH_4,i}} s_i N_i \tag{17}$$

Here, $h_{CH_4,i}$ is the mass transfer cofficient for the diffusion of methane from the gas phase to the surface of the particles, and the first term on the right hand side of Eqs. 15 and 17 accounts for the limitation of this transport on the heterogenous reaction rate.[16] The particle number sources due to heterogenous reaction are then

Table 1. Summary of Simulation Conditions

		Inlet Conditions				Tube Wall Conditions	
CH_4 (NL/min)	Ar (NL/min)	CH_4 Mole Fraction	Absolute Pressure (kPa)	Reynolds	Prandtl	Tube diameter (m)	Tube temperature (K)
3.73	3.73	0.5	41	740	0.664	0.015	1800

$$\left[\dot{N}_1\right]_{\text{het}} = -H_{\text{het},1}N_1 \tag{18}$$

$$\left[\dot{N}_i\right]_{\text{het}} = H_{\text{het},i-1}N_{i-1} - H_{\text{het},i}N_i \quad ; \quad i = 2,\ldots,M \tag{19}$$

The kinetic parameters reported by Patrianakos et al.[16] for first order homogenous and heterogenous decomposition of methane ($k_{0,\text{hom}} = 10^{14}$ 1/s, $E_{\text{a,hom}} = 400$ kJ/mol, $k_{0,\text{het}} = 2500$ m/s, and $E_{\text{a,het}} = 150$ kJ/mol) are used; these parameters were obtained by fitting the 1-D model of[16] to the experimental data of Rodat et al.[3] The particle population is assumed to undergo Brownian coagulation, which is modeled using Fuchs' coagulation coefficients $K_{i,j}$ for spherical particles,[42] which are valid in the kinetic, transition, and continuum regimes. In reality, whereas homogenous nucleation and heterogenous growth leads to the formation of small, approximately spherical primary particles, subsequent coagulation leads to the formation of aggregate particles having a fractal morphology composed of many primary particles. Modeling the Brownian coagulation of fractal aggregates, as well as other relevant phenomena such as thermal restructuring of the aggregates, is involved[43–45] and, therefore, for simplicity the coagulation of spherical particles is assumed here. The monomer number source due to coagulation of monomers with i-mers is

$$\left[\dot{N}_1\right]_{\text{coag}} = -\sum_{j=1}^{M} K_{1,j}N_1N_j \tag{20}$$

and the net i-mer number source due to coagulation is[46]

$$\left[\dot{N}_i\right]_{\text{coag}} = \sum_{j=1}^{i-1}\left(1-0.5\delta_{i-1,j}\right)\frac{2^{j-1}}{2^{i-1}-2^{i-2}}K_{i-1,j}N_{i-1}N_j \tag{21}$$

$$+\sum_{j=1}^{i}\left(1-0.5\delta_{i,j}\right)\frac{2^{i}-2^{i-1}-2^{j-1}}{2^{i}-2^{i-1}}K_{i,j}N_iN_j \tag{22}$$

$$-\sum_{j=1}^{M} K_{i,j}N_iN_j \quad ; \quad i = 2,\ldots,M \tag{23}$$

The volumetric particle species sources in Eq. 5 are then

$$R_1 = m_1\left(\left[\dot{N}_1\right]_{\text{hom}} + \left[\dot{N}_1\right]_{\text{het}} + \left[\dot{N}_1\right]_{\text{coag}}\right) \tag{24}$$

$$R_i = m_i\left(\left[\dot{N}_i\right]_{\text{het}} + \left[\dot{N}_i\right]_{\text{coag}}\right) \quad ; \quad i = 2,\ldots,M \tag{25}$$

Furthermore, the mean Planck radiation absorption coefficient of the particle population is

$$\kappa_p = \frac{\pi}{4}\sum_{i=1}^{M} Q_{\text{abs},i}d_i^2N_i \tag{26}$$

where $Q_{\text{abs},i}$ is the wavelength averaged absorption efficiency of the i-mer particles estimated via spectral integration over the wavelength range 0.8–7.5 μm using Mie theory.[16,47,48] All of the above terms are explained in greater detail in Ref. [16].

Computational Implementation of the Model

Numerical methods

The ANSYS Fluent commercial finite volume fluid dynamics solver is used to solve the transport Eqs. 2–5. In particular, the pressure-based solver is used, using the SIMPLE pressure velocity coupling method.[49] Gradients are computed using the least squares cell-based method, and the standard pressure interpolation scheme is used. The QUICK[50] scheme is used for the spatial discretization of the Navier–Stokes, energy transport, and species transport, equations. A second order upwind scheme is used for the RTE, and a first order upwind scheme is used for the species transport equations. Species transport is solved for CH_4, H_2 and the 46 particle species considered. The finite volume method is also used for the computation of radiation transport using a 4×4 discretization of the zenith and azimuth angles in each octant. The temperature and composition dependent thermo-physical properties of the gas phase are computed by user defined functions. The diffusivities, the particle and species mass sources, the radiation absorption coefficient and the total volumetric heterogenous reaction rate constant are also computed by a user defined function. The solution time is about 100 h on a modern PC workstation (parallel Fluent on a Quad Core processor at 2.93 GHz).

Computational domain

The chosen test case corresponds to the geometry and operating conditions of a reactor tube of an indirect heating mode, 50 kW solar TDM reactor developed by PROMES.[3] The reactor tube (henceforth referred to simply as the "reactor") is circular in cross section and is modeled using a structured 2-D axisymmetric grid. The grid is oriented such that the x-direction lies along the length of the reactor and the y-direction lies along the radius of the reactor. The diameter and length of the reactor are, respectively, 15 mm and 0.6 m. In the x-direction, a constant grid spacing $\Delta x = 6 \times 10^{-4}$ m is used, resulting in 1000 cells along the reactor. In the y-direction, a refined grid is used close to the wall, starting with $\Delta y = 10^{-5}$ m and increasing with a growth factor of 1.05 over the first 40 cells. A constant grid spacing of $\Delta y = 7 \times 10^{-5}$ m is used thereafter up to the axis of symmetry. The total number of cells in the domain is 1.3×10^5.

Figure 1. Sketch of the tubular TDM reactor: axisymmetric temperature field in the simulated TDM reactor with a real length to radius ratio (T ranging from 300 to 1800 K).

[Color figure can be viewed in online issue, which is available at wileyonlinelibrary.com.]

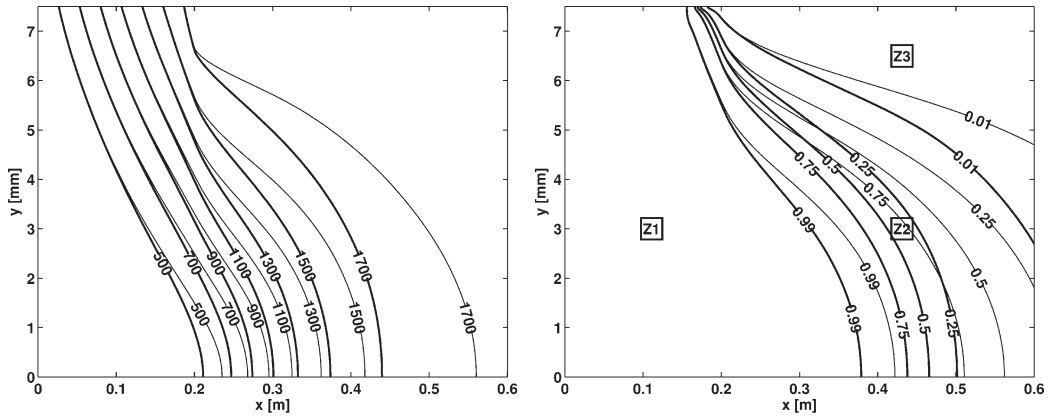

(a) Flow temperature (K) (b) Scaled methane mole fraction

Figure 2. Isocontours of (a) flow temperature and (b) scaled methane mole fraction [$X_{CH_4}/X_{CH_4}(x = 0)$].

The thick and thin lines depict, respectively, results with and without radiation transport.

Although not discussed in detail, a grid sensitivity study was performed before selecting the present discretization.

Boundary conditions

The feed gas conditions for the reactor are 3.73 dm^3/min of methane and 3.73 dm^3/min of argon at 101325 Pa and 273.15 K, and, consequently, the inlet boundary conditions for the gas phase are a methane molar fraction of $X_{CH_4}(x = 0) = 0.5$ and a gas velocity of 0.77214 m/s at 300 K and 101325 Pa; as such, the flow is laminar (Table 1). A zero concentration gradient boundary condition is specified for methane and hydrogen along the walls of the reactor, and a constant pressure boundary condition is specified at the outlet. The particle species concentrations at the inlet and along the wall are set to zero (i.e., Brownian diffusion deposition of the particles on the wall is modeled), whereas at the outlet the concentration gradient is set to zero. The reactor wall is separated into two zones, $0 < x \leq 0.2$ m and $0.2 < x \leq 0.6$ m, in the first of which the wall temperature increases linearly from 300 to 1800 K and in the second of which it remains constant at 1800 K. The wall emissivity is set to 0.9, corresponding to the emissivity of graphite at high temperature.

Verification

Mass and energy conservation in the computational domain have been verified for the overall reactor model, and particle mass and number conservation have been verified separately for the particle model. Furthemore, kinetic parameters are used which have been extracted from experimental results using the validated 1-D reactor model of Patrianakos et al.,[16] which uses the same particle model. The aim of the present work is to describe the formulation of the 2-D reactor model and to use it to study on a qualitative basis the radiation absorption and particle growth phenomena in an experimental reactor; in this respect, the model enables the particle size distribution to be resolved locally throughout the reactor, something which is not possible experimentally. Validation of the model against experimental methane conversion results and experimental particle size distributions obtained from transmission electron microscopy of experimental particle populations, as well as comparison with the 1-D model of Patrianakos et al.[16] will be described in a future work. However, presently, it is noted that the predicted methane conversion is in agreement with the experimental results reported in Ref. [3].

Results and Discussion

A sketch of the reactor is shown in Figure 1 to scale. The aspect ratio of the reactor (length to radius ratio) is 80 and so it is not possible to depict field variables inside the reactor to scale clearly; therefore, in the following all field variables are plotted with the radius scale (y axis) enlarged.

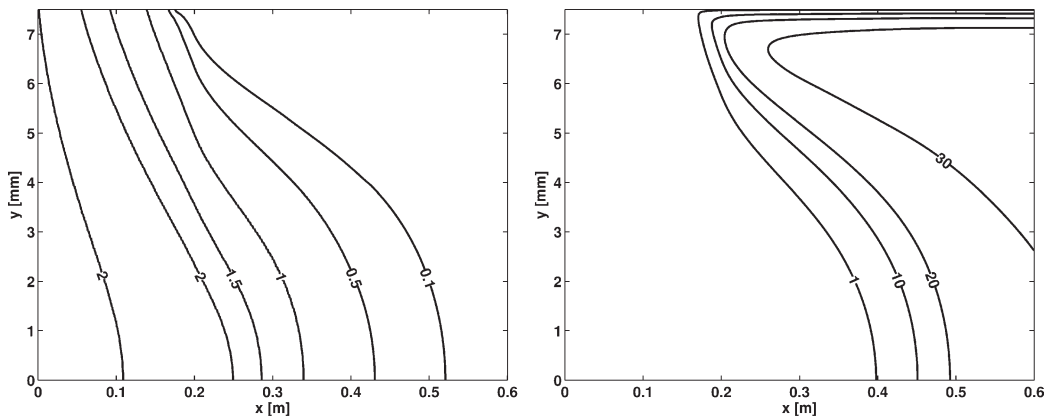

(a) κ_{CH_4} (b) κ_p

Figure 3. Isocontours of the absorption coefficient (a) κ_{CH_4} and (b) κ_p (1/*m*).

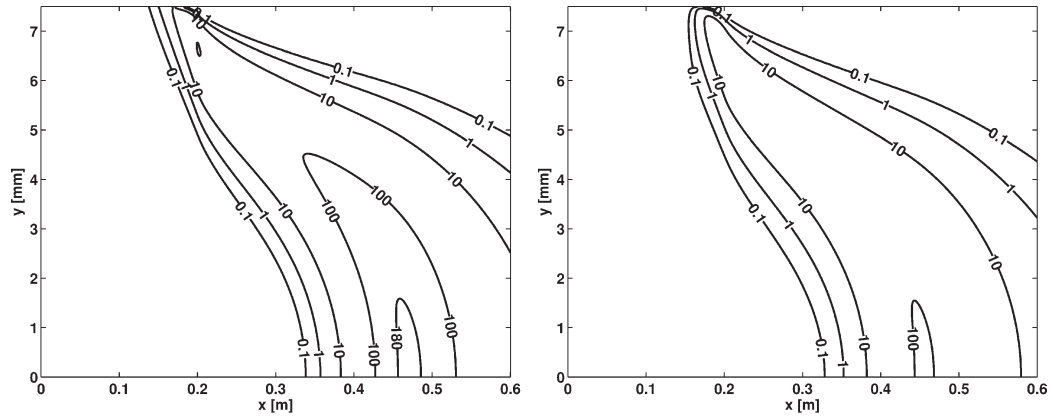

(a) $R_{\mathrm{CH_4,hom}}$ (b) $R_{\mathrm{CH_4,het}}$

Figure 4. Isocontours of (a) homogenous and (b) heterogenous volumetric methane reaction rate (mol/m^3/s).

The simulation results are presented below in Figures 2–10, and the effects of radiation and particle transport in the reactor are discussed. Several field variables are depicted using isocontour plots. Given the very large aspect ratio of the reactor, to correctly interpret the geometry of the inter-contour regions it is necessary to consider that the axial distance between contours is 80 times greater than depicted, whereas gradients with even a small apparent radial component are essentially radial.

Effect of radiation transport

The effect of radiation transport in the reactor can be seen by comparing results with and without the inclusion of the radiative heat transfer model: the absence of radiation

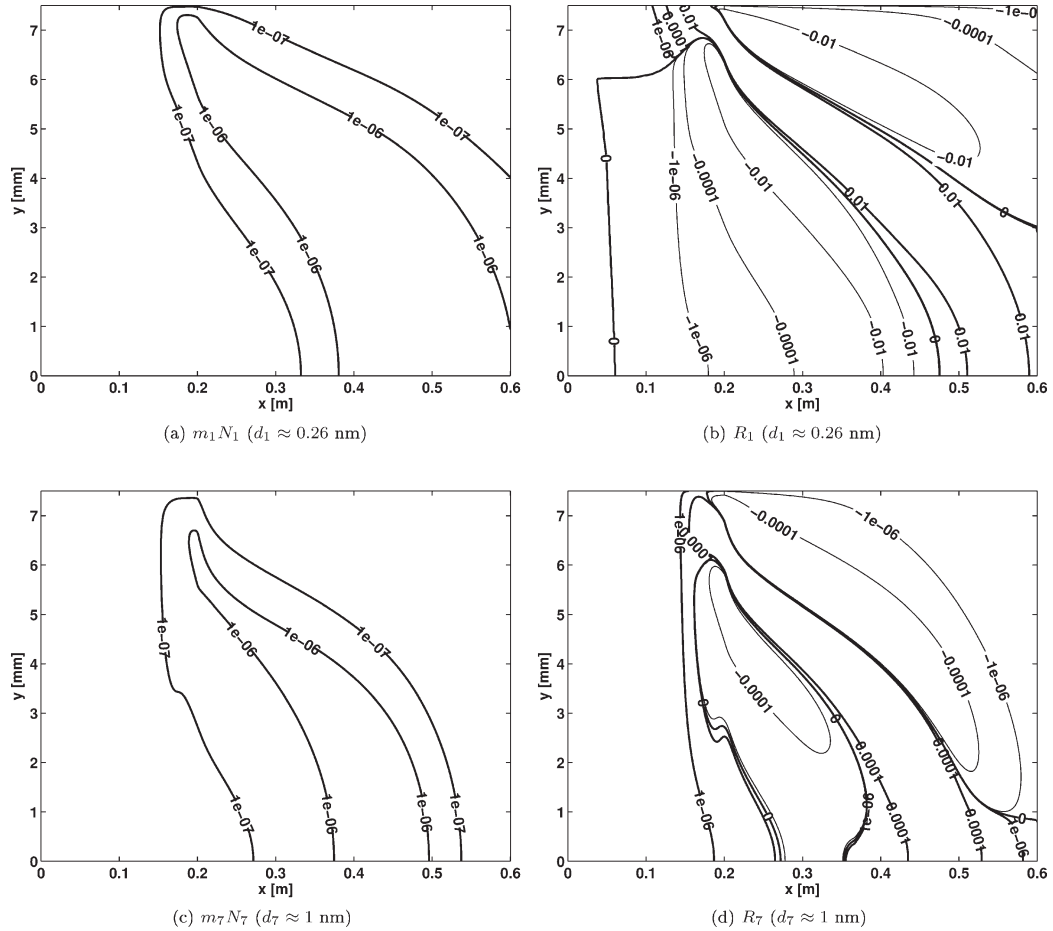

(a) m_1N_1 ($d_1 \approx 0.26$ nm) (b) R_1 ($d_1 \approx 0.26$ nm)

(c) m_7N_7 ($d_7 \approx 1$ nm) (d) R_7 ($d_7 \approx 1$ nm)

Figure 5. Local particle mass concentration (m_i N_i in $\neq$/m^3, left column) and volumetric mass source (R_i in kg/m^3/s, right column) for various sections or, equivalently, particle diameters (d_i in nm).

A positive value of R_i corresponds to a net source of particles in the ith section, considering particles entering the section due to coagulation and heterogenous growth of smaller particles, as well as particles leaving the section due to own coagulation with other particles and heterogenous growth; in the case of the first section, R_1 also includes particle nucleation. (continued in Figure 6).

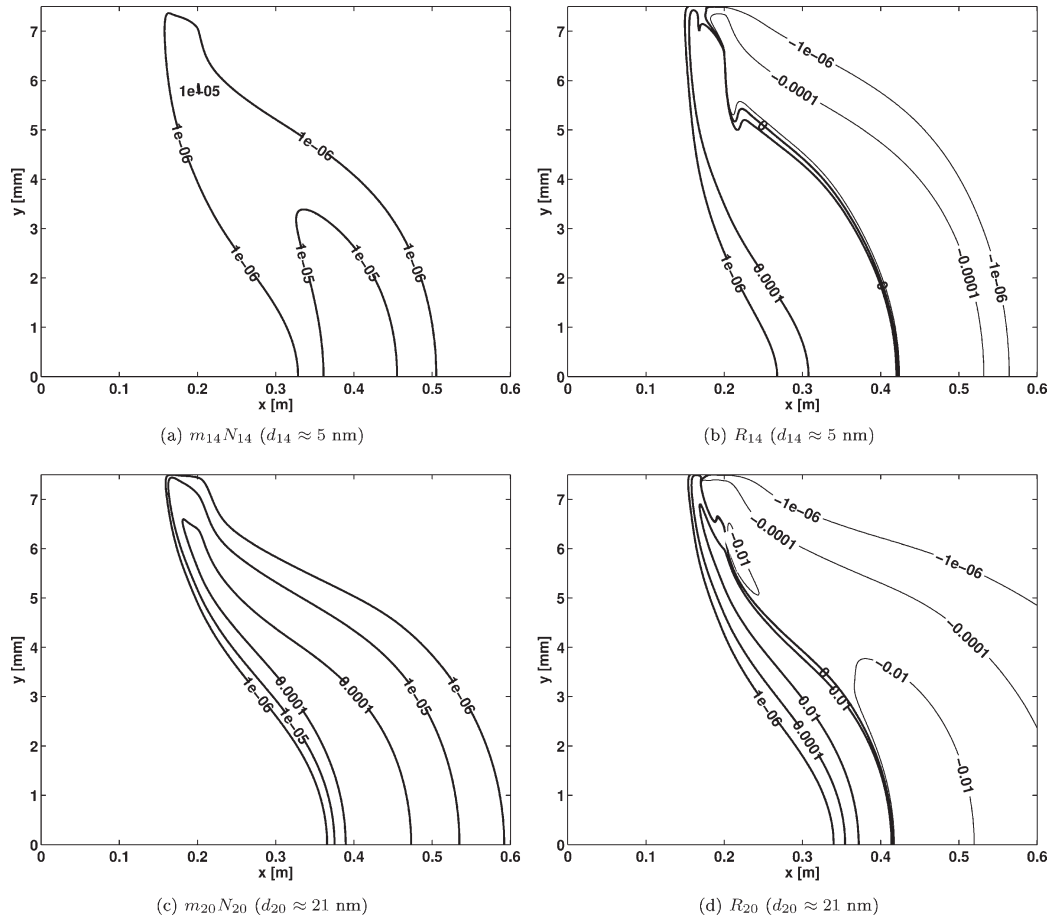

(a) $m_{14}N_{14}$ ($d_{14} \approx 5$ nm)

(b) R_{14} ($d_{14} \approx 5$ nm)

(c) $m_{20}N_{20}$ ($d_{20} \approx 21$ nm)

(d) R_{20} ($d_{20} \approx 21$ nm)

Figure 6. Continuation of Figure 5.

transport implies the neglect of radiation absorption and emission by the graphite wall of the reactor, particles, and methane. As the wall temperature is high (1800 K for $x >$ 0.2 m), the flow is heated by convective and radiative heat transfer because both methane and carbon particles absorb radiation in the infrared region. Although it is not reported here, the assumption of a nonscattering medium was validated based on the value of the scattering *albedo* which is lower than 0.1 throughout the reactor except in the vicinity of the reactor wall (about 1 mm) where its value remains lower than 0.2. Because of the small optical thicknesses involved and the weak value of the scattering *albedo*, the influence of scattering may be neglected. A discussion about the effect of scattering in solid–gas suspensions can be found in Ref. [51]. Figures 2a, and b show, respectively, isocontours of flow temperature (the gas particle mixture is assumed to be in thermal equilibrium) and a scaled methane mole fraction $[X_{CH_4}/X_{CH_4}(x = 0))]$, with and without radiation transport, from which the development of a reaction boundary layer inside the reactor is evident. In particular, on the basis of Figure 2b, the flow can be distiguished into three zones: the first zone (Z1), encompassing the flow outside the reaction boundary layer, corresponds to the preheating zone in which the methane is heated to a temperature at which significant reaction commences ($\sim$ 1500 K); the second zone (Z2), encompassing the flow in the outer region of the reaction boundary layer, corresponds to the reaction zone in which conversion proceeds from 0.01 to 0.99 as methane is transported from Z1 to Z2 and heat is transported from the wall to Z3 and then to Z2; the third zone (Z3), encompassing the flow in the inner region of the reaction boundary layer, corresponds to the post reaction zone in which the flow consists mainly of the reaction products, i.e., hydrogen and carbon particles. As the flow is laminar, Z1, Z2, and Z3 are relatively well defined along the length of the reactor.

From Figures 2a, b it is evident that radiation absorption by methane in the preheating zone (Z1) increases the rate of heat transfer to the flow, shifting the reaction zone (Z2) upstream and thickening the reaction boundary layer. To highlight the relative contribution of the methane and of the particles to radiation absorption, isocontours of the absorption coefficient of methane and of the particles are shown in Figures 3a and b, respectively: in Z2 the coefficient of methane decreases while the coefficient of particles increases as methane is converted; furthermore, the particles absorption coefficient in Z3 is an order of magnitude greater than that of methane in Z1, and in the outer region of the reaction boundary layer (near the interface between Z1 and Z2) the coefficients are similar due to the presence of small particles. Consequently, the three reactor zones also correspond to three radiation zones: in Z1 radiation is absorbed mostly by methane, in Z2 radiation is absorbed by both methane and carbon particles, whereas in Z3 radiation is absorbed mostly by particles and methane absorption is negligible.

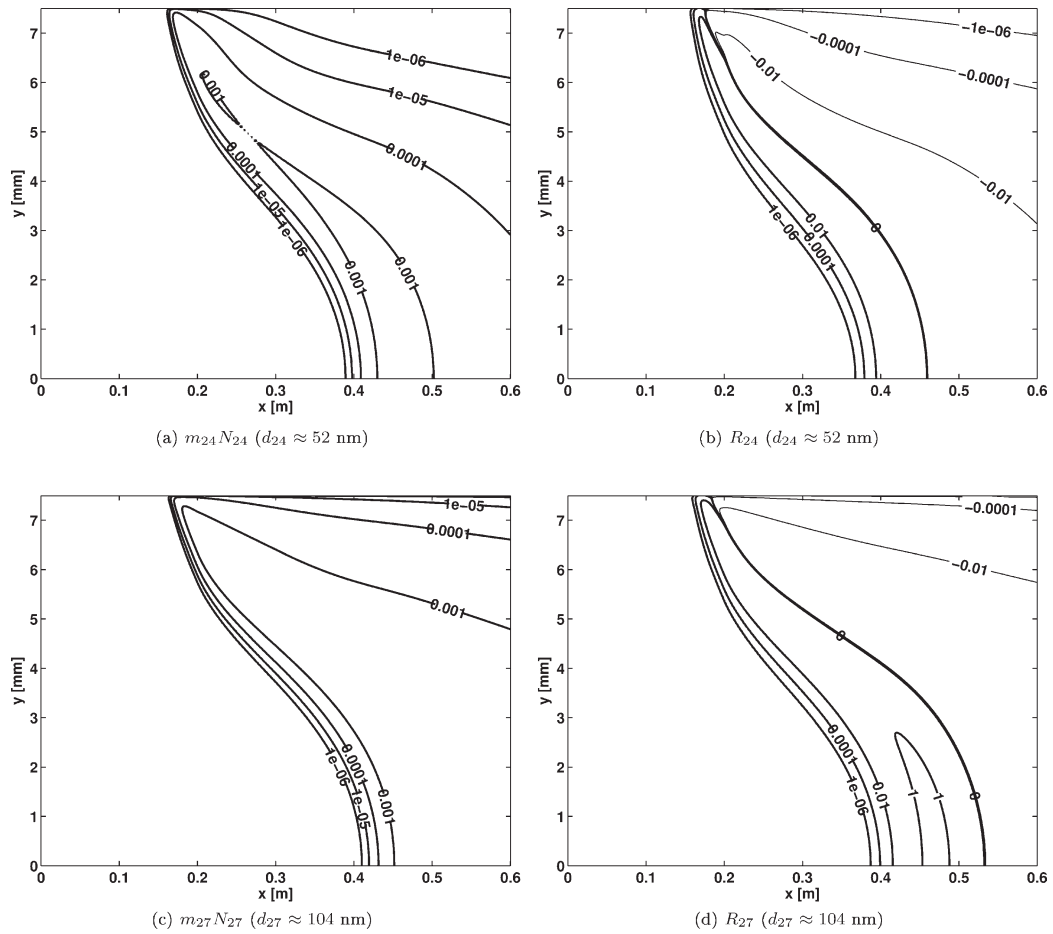

Figure 7. Continuation of Figure 6.

Particle transport

The local volumetric homogenous and heterogenous reaction rates are shown in Figure 4. Because of their underlying Arrhenius dependence and first order behavior, both the homogenous and heterogenous rates increase with the temperature increase across the outer region of the reaction boundary layer, and then they decrease with the decrease in methane mole fraction across the inner region of the reaction boundary layer. The heterogenous rate also depends on the total particle surface area which apparently suffices to ensure a heterogenous rate similar to the homogenous rate; however, in this regard it is noted that the simulated balance between homogenous and heterogenous reaction is very sensitive to the assumed kinetic parameters.

Figures 5–7 show the local mass concentration (m_iN_i) and volumetric mass source (R_i) of particles in several sections. A positive value of R_i corresponds to a net source of particles in the ith section, considering particles entering the section due to coagulation and heterogenous growth of smaller particles, as well as particles leaving the section due to own coagulation with other particles and heterogenous growth; in the case of the first section, R_1 also includes particle nucleation. Figures 5–d indicate that an excess of small particles, having diameters of the order of a few nm, is produced in the reaction zone (Z2; $R_i > 0$), which then diffuse into the preheating zone (Z1) and also into the post reaction zone (Z3), where they are consumed by coagulation ($R_i < 0$); because of their large diffusivity, the transport of the small particles is diffusion dominated and their mass concentration is relatively uniform throughout the region of their existense. Figures 6–d then indicate that the small particles in Z1 coagulate, producing an excess of medium sized particles ($R_i > 0$) having diameters of the order of a few tens of nanometer, which being less diffusive are advected back into Z2 and Z3, where they are consumed by heterogenous reaction and coagulation ($R_i < 0$); because of their moderate diffusivity, the transport of the medium sized particles is advective–diffusive. Finally, Figures 8–d indicate that large particles, having diameters of the order of a few hundreds of nanometer, are produced mostly in Z3 from the coagulation of small and medium sized particles ($R_i > 0$); because of their low diffusivity, the transport of the large particles is advection dominated, and there is little transport of these particles perpendicular to the flow direction.

Figure 9 shows the number-based size diameter distribution of the particles at various axial and radial positions in the reactor, from which it is evident that apart from the expected variation in the distributions axially along the reactor there is also a significant variation radially across the reactor. The pattern in the evolution of the distribution along the four loci of constant radial position is similar: in the preheating zone (Z1), the nucleation rate is very small due to the low temperature, only a few small particles are formed, and the distribution is unimodal; in the reaction zone (Z2),

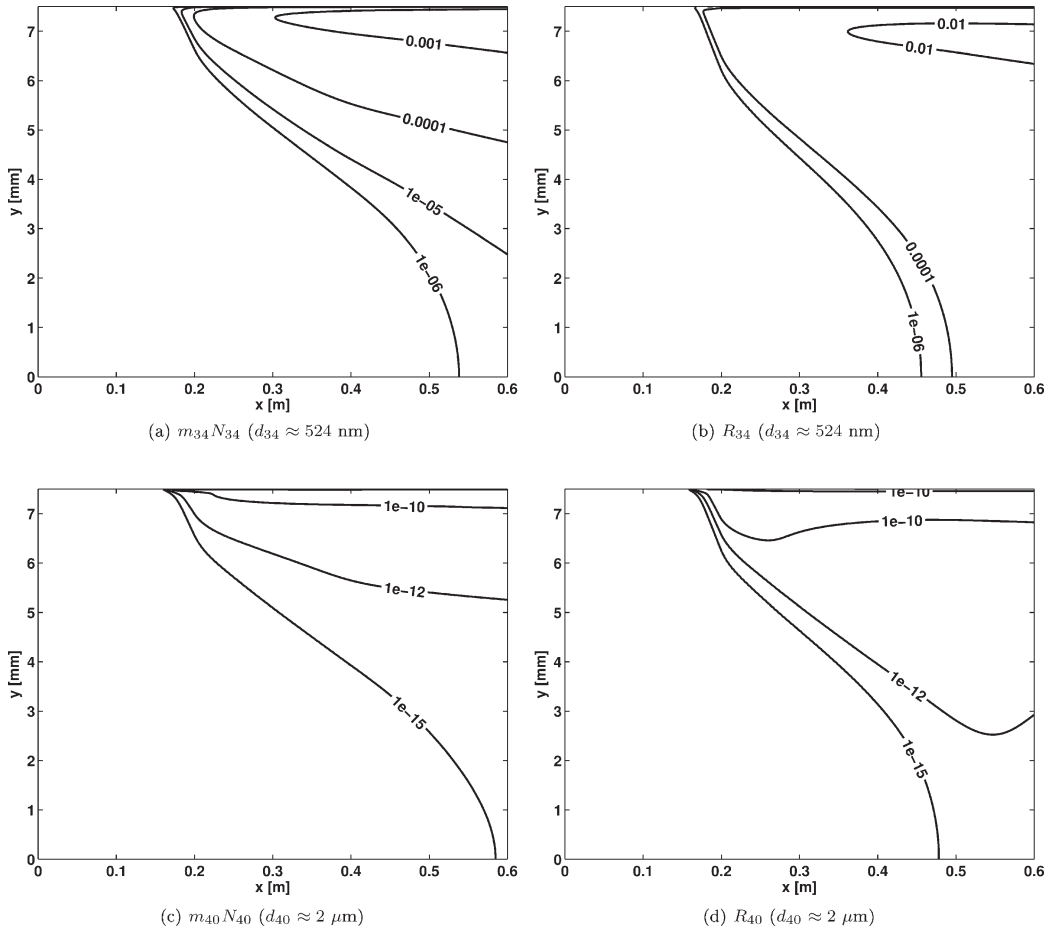

(a) $m_{34}N_{34}$ ($d_{34} \approx 524$ nm) (b) R_{34} ($d_{34} \approx 524$ nm)

(c) $m_{40}N_{40}$ ($d_{40} \approx 2$ μm) (d) R_{40} ($d_{40} \approx 2$ μm)

Figure 8. Continuation of Figure 7.

the nucleation rate is large, many particles are formed, the size of the particles increases due to heterogenous growth and coagulation, the distribution expands into large number concentrations and large particle diameters, and it becomes bimodal; finally, in the post reaction zone (Z3), the nucleation and heterogenous growth rates are very small due to the low methane concentration, the small particles are depleted via coagulation, the distribution contracts into smaller number concentrations and expands into larger particle diameters, and it becomes unimodal again. The bimodality of the distribution in Z2 reflects the competition between nucleation, on the one hand, and heterogenous growth and coagulation, on the other hand, whereas the unimodality of the distribution in Z3 results from the coagulation ageing process. With reference to Figure 2b, near the wall of the reactor the axial extent of the reaction zone is small and the zone is situated closer to the inlet of the reactor, whereas near the centerline of the reactor the reaction zone is more extensive and it is situated further along the reactor. Consequently, there is a lag in the evolution of the local distribution along loci of constant radial position near the centerline of the reactor in comparison to near the wall, although the pattern in the evolution is similar. This occurs because the flow is laminar and because, although the diffusivity of the small particles is large and so they are able to diffuse radially, the diffusivity of the large particles is small and therefore they follow the flow; thus, the evolution of the local distribution becomes radially independent as the distribution moves into large particle diameters.

Figure 10 shows the so called "mixing cup" average number-based diameter distribution of the particles at various axial positions along the reactor; this is the size distribution that would be obtained if the reactor were cut at the respective axial position and all the particles were collected as is. The pattern in the evolution of the mixing cup average distribution along the reactor is similar that of the local distribution; however, the mixing cup average distribution at the outlet of the reactor is still bimodal since near the centerline of the reactor the reaction zone extends all the way to the outlet of the reactor.

Conclusion

A 2-D model of methane thermal decomposition reactors has been described which accounts for flow, energy and species transport, as well as radiative heat transfer and carbon particle growth. Preliminary simulation results for a laminar flow reactor tube of the 50 kW PROMES reactor indicate the existence of three distinct zones inside the tube, the preheating (Z1), reaction (Z2), and postreaction (Z3) zones. A detailed understanding is gained from the simulation results regarding particle growth and radiation absorption phenomena in each zone and their influence on the extent of the zones in the tube. In particular, radiation absorption is found to shift the reaction (Z2) zone upstream, and, due to the laminar flow conditions, it is found that the particle size distribution varies significantly across the diameter of the tube. Detailed information of this kind is valuable for future optimization of the TDM reactor and justifies the adopted

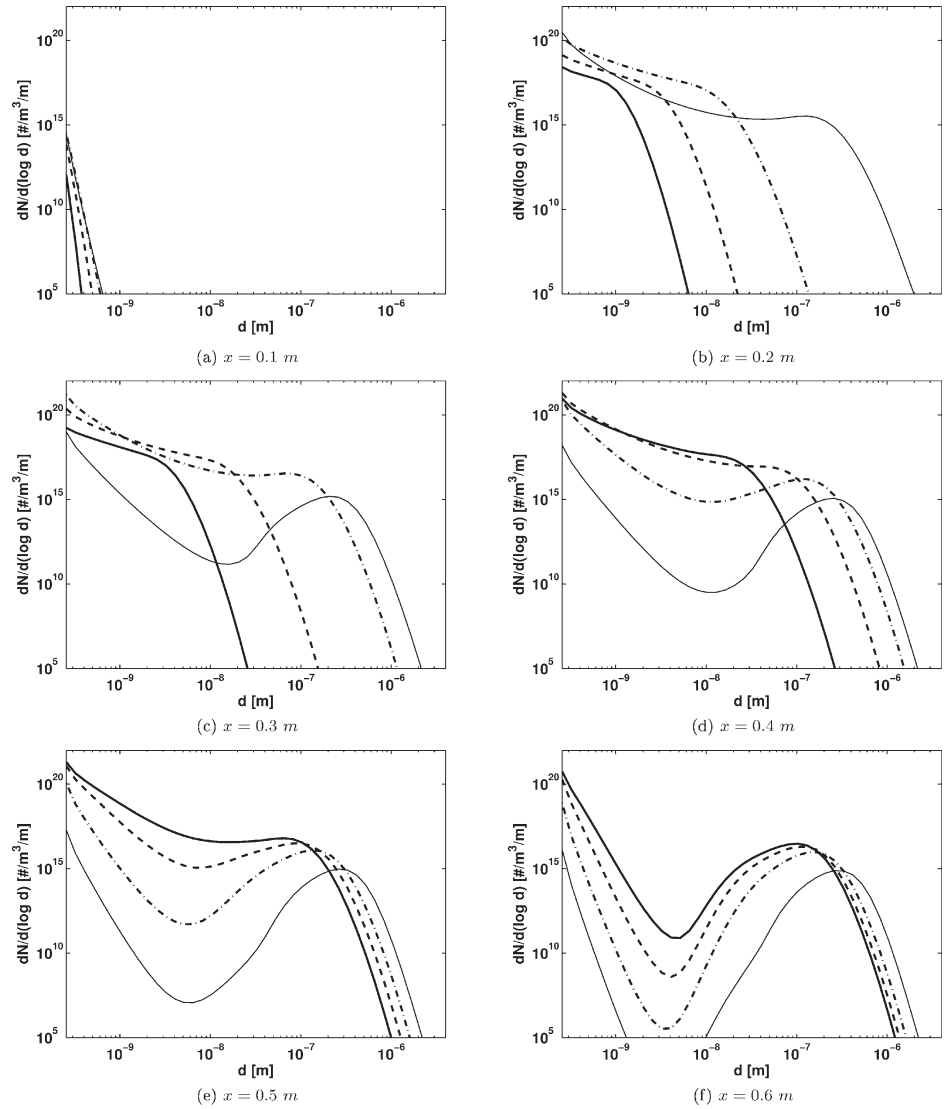

Figure 9. Local number-based diameter distribution of the particles at various axial (*x*) and radial (*y*) positions in the reactor.

Thick solid lines, $y = 0.0$ mm; dashed lines, $y = 3.0$ mm; dashed dotted lines, $y = 5.0$ mm; thin solid lines, $y = 7.5$ mm.

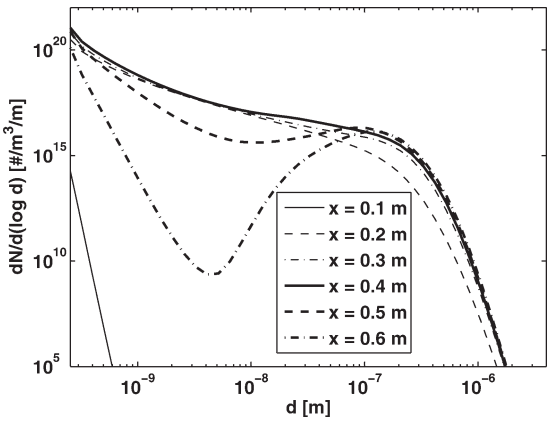

Figure 10. Mixing cup average number-based diameter distribution of the particles at various axial positions along the reactor; this is the size distribution that would be obtained if the reactor were cut at the respective axial position and all the particles were collected as is.

multidimensional approach. Furthermore, the model provides much scope for the inclusion of additional relevant transport phenomena, such as heterogenous reaction on the walls of the reactor and thermophoretic transport of the particles. Further work includes validation of the model against experimental methane conversion results, comparison with a 1-D model, and validation against particle size distributions obtained from transmission electron microscopy of experimental particle populations. Following this, the model can be used for reactor design optimization.

Acknowledgments

This work was funded in part by the European Commission under the SOLHYCARB project (contract number SES-CT2006-19770).

Literature Cited

1. Steinfeld A. Solar thermochemical production of hydrogen–a review. *Sol Energy*. 2005;78:603–615.
2. Rodat S, Abanades S, Sans J-L, Flamant G. Hydrogen production from solar thermal dissociation of natural gas: development of a 10 kW solar chemical reactor prototype. *Sol Energy*. 2009;83:1599–1610.

3. Rodat S, Abanades S, Sans J-L, Flamant G. A pilot-scale solar reactor for the production of hydrogen and carbon black from methane splitting. *Int J Hydrogen Energy*. 2010;35:7748–7758.
4. Dahl JK, Buechler KJ, Weimer AW, Lewandowski A, Bingham C. Solar-thermal dissociation of methane in a fluid-wall aerosol flow reactor. *Int J Hydrogen Energy*. 2004;29:725–736.
5. Dahl JK, Buechler JK, Finley R, Stanislaus T, Weimer AW, Lewandowski A, Bingham C, Smeets A, Schneider A. Rapid solar-thermal dissociation of natural gas in an aerosol flow reactor. *Energy*. 2004;29:715–725.
6. Kogan M, Kogan A. Production of hydrogen and carbon by solar thermal methane splitting. I. The unseeded reactor. *Int J Hydrogen Energy*. 2003;28:1187–1198.
7. Kogan A, Kogan M, Barak S. Production of hydrogen and carbon by solar thermal methane splitting. II. Room temperature simulation tests of seeded solar reactor. *Int J Hydrogen Energy*. 2004;29:1227–1236.
8. Kogan A, Kogan M, Barak S. Production of hydrogen and carbon by solar thermal methane splitting. III. Fluidization, entrainment and seeding powder particles into a volumetric solar receiver. *Int J Hydrogen Energy*. 2005;30:35–43.
9. Hirsch D, Steinfeld A. Solar hydrogen production by thermal decomposition of natural gas using a vortex-flow reactor. *Int J Hydrogen Energy*. 2004;29:47–55.
10. Maag G, Zanganeh G, Steinfeld A. Solar thermal cracking of methane in a particle-flow reactor for the co-production of hydrogen and carbon. *Int J Hydrogen Energy*. 2009;34:7676–7685.
11. Dahl JK, Barocas VH, Clough DE, Weimer AW. Intrinsic kinetics for rapid decomposition of methane in an aerosol flow reactor. *Int J Hydrogen Energy*. 2002;27:377–386.
12. Trommer D, Hirsch D, Steinfeld A. Kinetic investigation of the thermal decomposition of CH4 by direct irradiation of a vortex-flow laden with carbon particles. *Int J Hydrogen Energy*. 2004;29:627–633.
13. Wyss J, Martinek J, Kerins M, Dahl J, Weimer A, Lewandowski A, Bingham C. Rapid solar-thermal decarbonization of methane in a fluid-wall aerosol flow reactor fundamentals and application. *Int J Chem React Eng*. 2007;5:A69.
14. Rodat S, Abanades S, Coulie J, Flamant G. Kinetic modelling of methane decomposition in a tubular solar reactor. *Chem Eng J*. 2009;146:120–127.
15. Rodat S, Abanades S, Flamant G. High-temperature solar methane dissociation in a multitubular cavity-type reactor in the temperature range 1823–2073 K. *Energy Fuels*. 2009;23:2666–2674.
16. Patrianakos G, Kostoglou M, Konstandopoulos A. One-dimensional model of solar thermal reactors for the co-production of hydrogen and carbon black from methane decomposition. *Int J Hydrogen Energy*. 2011;36:189–202.
17. Ozalp N, Shilapuram V. Step-by-step methodology of developing a solar reactor for emission-free generation of hydrogen. *Int J Hydrogen Energy*. 2010;35:4484–4495.
18. Abanades S, Flamant G. Experimental study and modeling of a high-temperature solar chemical reactor for hydrogen production from methane cracking. *Int J Hydrogen Energy*. 2007;32:1508–1515.
19. Dahl JK, Weimer AW, Krantz WB. Sensitivity analysis of the rapid decomposition of methane in an aerosol flow reactor. *Int J Hydrogen Energy*. 2004;29:57–65.
20. Hirsch D, Steinfeld A. Radiative transfer in a solar chemical reactor for the co-production of hydrogen and carbon by thermal decomposition of methane. *Chem Eng Sci*. 2004;59:5771–5778.
21. Maag G, Lipinski W, Steinfeld A. Particle-gas reacting flow under concentrated solar irradiation. *Int J Heat Mass Transfer*. 2009;52:4997–5004.
22. Chen SHP, Saxena SC. Thermal conductivity of argon in the temperature range 350 to 2500 K. *Mol Phys*. 1975;29:455–466.
23. Roine A. *Chemical Reaction and Equilibrium Software with Extensive Thermochemical Database*. Pori, Finland: Outokumpu Research Oy, New York, 2002.
24. Component Plus software, Windows version 3.4, ProSim, France.
25. Bird RB, Stewart WE, Lightfoot EN. *Transport Phenomena*. New York: Wiley, 2002.
26. Seinfeld JH, Pandis SN. *Atmospheric Chemistry and Physics: From Air Pollution to Climate Change*. New York: Wiley, 1998.
27. Modest MF. *Radiative Heat Transfer*. New York: McGraw-Hill, 1993.
28. Raithby GD, Chui EH. A finite-volume method for predicting a radiant heat transfer in enclosures with participating media. *ASME J Heat Transfer*. 1990;112:415–423.
29. Caliot C, Abanades S, Soufiani A, Flamant G. Effects of non-gray thermal radiation on the heating of a methane laminar flow at high temperature. *Fuel*. 2009;88:617–624.
30. Taine J, Soufiani A. Gas IR radiative properties, from spectroscopic data to approximate models. *Adv Heat Transfer*. 1999;33:295–341.
31. Perrin MY, Soufiani A. Approximate radiative properties of methane at high temperature. *J Quant Spectros Radiat Transfer*. 2007;103:3–13.
32. Rigopoulos S. Population balance modeling of polydispersed particles in reactive flows. *Prog Energy Combust Sci*. 2010;36:412–443.
33. Pratsinis SE. Simultaneous nucleation, condensation, and coagulation in aerosol reactors. *J Colloid Interface Sci*. 1988;124:416–427.
34. Xiong Y, Pratsinis SE. Gas phase production of particles in reactive turbulent flows. *J Aerosol Sci*. 1991;22:637–655.
35. Tree DR, Svensson KI. Soot processes in compression ignition engines. *Prog Energy Combust Sci*. 2007;33:272–309.
36. Frenklach M, Wang H. *Detailed modeling of soot particle nucleation and growth*. In: *Proceedings of the 23rd International Symposium on Combustion*. Orleans, France, 1990:1559–1566.
37. Richter H, Granata S, Green WH, Howard JB. Detailed modelling of PAH and soot formation in a laminar premixed benzene/oxygen/argon low-pressure flame. *Proc Combust Inst*. 2005;30:1397–1405.
38. Tao F, Reitz RD, Foster DE, Liu Y. Nine-step phenomenological diesel soot model validated over a wide range of engine conditions. *Int J Therm. Sci*. 2009;48:1223–1234.
39. Tao F, Golovitchev VI, Chomiak J. *Application of complex chemistry to investigate combustion zone structure of DI diesel sprays under engine like conditions*. In: *Proceedings of the COMODIA*, Nagoya, Japan, 2001. 2001:92–100.
40. Hong S, Wooldridge MS, Im HG, Assanis DN, Pitsch H. Development and application of a comprehensive soot model for 3D CFD reacting flow studies in a diesel engine. *Combust Flame*. 2005;143:11–16.
41. Kostoglou M, Karabelas AJ. Evaluation of zero order methods for simulating particle coagulation. *J Colloid Interface Sci*. 1994;163:420–431.
42. Fuchs NA. *The Mechanics of Aerosols*. New York: Pergamon Press, 1964.
43. Di Stasio S, Konstandopoulos AG, Kostolgou M. Cluster-cluster aggregation kinetics and primary particle growth of soot nanoparticles in flame by light scattering and numerical simulations. *J Colloid Interface Sci*. 2002;247:33–46.
44. Kostoglou M, Konstandopoulos AG, Friedlander SK. Bivariate population dynamics simulation of fractal aerosol aggregate coagulation and restructuring. *J Aerosol Sci*. 2006;37:1102–1115
45. Kostoglou M, Konstandopoulos AG. Evolution of aggregate size and fractal dimension during Brownian coagulation. *J Aerosol Sci*. 2001;32:1399–1420.
46. Kostoglou M, Karabelas AJ. Evaluation of numerical methods for simulating an evolving particle size distribution in growth processes. *Chem Eng Commun*. 1995;136:177–199.
47. Bohren CF, Huffman DR. *Absorption and Scattering of Light by Small Particles*. Wiley, 1998.
48. Klein HH, Karni J, Ben-Zvi R, Bertocchi R. Heat transfer in a directly irradiated solar receiver/reactor for solid-gas reactions. *Sol Energy*. 2007;81:1227–1239.
49. Patankar SV, Spalding BD. A calculation procedure for heat, mass and momentum transfer in three-dimensional parabolic flows. *Int J Heat Mass Transfer*. 1972;15:1787–1806.
50. Leonard BP, Mokhtari S. ULTRA-SHARP Nonoscillatory Convection Schemes for High-Speed Steady Multidimensional Flow. Technical Memorandum 102568 (ICOMP-90-12), NASA Lewis Research Center, Cleveland, 1990.
51. Caliot C, Eymet V, El Hafi M, Le Maoult Y, Flamant G. Parametric study of radiative heat transfer in participating gas-solid flows. *Int J Thermal Sci*. 2008;47:1413–1421.

Manuscript received Mar. 8, 2011, and revision received July 26, 2011.